

Second-order correlations in directed emissions in sodium atoms

Ara Tonoyan

Institute for Physical Research, National Academy of Sciences of Armenia, 0204 Ashtarak, Armenia

Sushree Subhadarshinee Sahoo

Johannes Gutenberg-Universität Mainz, 55128 Mainz, Germany

Helmholtz-Institut Mainz, 55099 Mainz, Germany and

Department of Physics, Indian Institute of Technology, Kanpur, Kanpur 208016, India

Anahit Gogyan*

Institute for Physical Research, National Academy of Sciences of Armenia, 0204 Ashtarak, Armenia

Oleg Tretiak and Razmik Aramyan

Johannes Gutenberg-Universität Mainz, 55128 Mainz, Germany and

Helmholtz-Institut Mainz, 55099 Mainz, Germany

Alexander Akulshin

Optical Sciences Centre, Swinburne University of Technology, Melbourne 3122, Australia

Dmitry Budker

Johannes Gutenberg-Universität Mainz, 55128 Mainz, Germany

Helmholtz-Institut Mainz, 55099 Mainz, Germany

GSI Helmholtzzentrum für Schwerionenforschung GmbH, 64291 Darmstadt, Germany and

Department of Physics, University of California, Berkeley, California 94720, USA

(Dated: November 18, 2025)

We report on measurements of second-order intensity correlations $g^{(2)}(\tau)$ of infrared emission under bichromatic excitation at 589.2 nm and 569.0 nm of sodium atoms contained in a buffer-gas-free and uncoated 10-cm-long vapor cell. Directional emissions at $2.34 \mu\text{m}$ in the forward direction and $2.21 \mu\text{m}$ in both forward and backward directions under different experimental parameters are considered for this study. The measured values of $g^{(2)}(0)$ in all cases are found to exceed unity, while remaining significantly below the thermal light limit of 2. Cross-correlation measurements reveal that forward- and backward-propagating $2.21 \mu\text{m}$ radiations are correlated. Oscillatory features in $g^{(2)}(\tau)$ are observed over a broad range of excitation powers, and the dependence of the oscillation frequency on laser power can be attributed to AC Stark shifts, with contributions from hyperfine atomic structure in selected atomic velocity groups even in the presence of Doppler broadening. Our study establishes that the observed mid-infrared emission arises from a phase-matched, continuous-wave cooperative process that combines features of lasing and collective amplified spontaneous emission. The results highlight the buildup of long-range dipole coherence and velocity-selective coupling of atomic groups, which together govern the observed photon correlations and forward-backward emission symmetry. The demonstrated backward emission is of particular interest for applications in laser guidestar generation and mesospheric remote sensing, where understanding the statistical properties of the emitted light is essential for optimizing sodium-based light sources.

I. INTRODUCTION

Coherent and nonlinear optical processes in alkali vapors have a long and rich history, closely linked to the development of laser technology [1–3].

This progress has enabled the discovery and detailed study of a wide range of phenomena, including Amplified Spontaneous Emission (ASE), Superradiance and Superfluorescence, Stimulated Electronic Raman Scattering (SERS), Four-Wave Mixing (FWM), and others [4–11].

Among these optical processes, mirrorless lasing (ML) in atomic vapors represents a particularly striking example, in which directional coherent emission arises without the use of conventional optical cavities or mirrors. In this case, the required feedback originates from ASE or distributed feedback within the medium itself, typically supported by population inversion in specific atomic levels. The term "mirrorless lasing" is sometimes extended to encompass stimulated emission processes that exhibit a distinct pump threshold and spectral narrowing, yet result in a state of relatively low temporal coherence when compared to conventional cavity-based lasers [12].

* agogyan@gmail.com

Mirrorless lasing simplifies the design of light sources

and makes them attractive for applications in remote sensing, atomic clocks, and precision metrology [13]. It is particularly useful for stand-off detection of atmospheric pollutants, trace gases, or environmental parameters [14]. Its high sensitivity, spectral selectivity, and potential for compact, alignment-free setups open pathways for portable and field-deployable sensing technologies [15, 16].

Mirrorless lasing in atomic vapors has been realized in various configurations. It was observed for the first time in Cs vapors in Ref. [17] and followed by a number of experiments in alkali vapors leading to pulsed [4, 18] and continuous-wave (CW) lasing [19]. Degenerate mirrorless lasing was experimentally observed in forward direction in a dilute rubidium vapor under single-linearly polarized CW excitation of the D₂ cycling transitions, characterized by orthogonally polarized emission above a $\sim 3 \text{ mW/cm}^2$ threshold and a sharp magnetic field sensitive resonance [20]. Non-degenerate ML was observed at $5.2 \mu\text{m}$ in Rb vapors that are stepwise excited by low-power CW resonant light [21]. In Ref. [22] backward-directed continuous-wave emission at $2.21 \mu\text{m}$ from sodium vapor via two-photon excitation of the $3S_{1/2} \rightarrow 4D_{5/2}$ transition was demonstrated, achieving a sub 10 mW threshold. Later, polychromatic ML in hot cesium vapor was observed by pumping the $6S_{1/2} \rightarrow 8P_{3/2}$ line, producing at least seven infrared emissions and two blue emissions [23]. This directional blue emission is due to FWM, as there is no population inversion on these transitions, so ASE does not occur. Recent theoretical studies predicted degenerate mirrorless lasing in warm alkali vapors, identifying a Doppler-resilient gain sideband under linearly polarized two-level pumping and outlining conditions for sustained inversion-enhanced gain [24, 25]. Spectral properties of ML, such as temporal coherence and linewidth, can be estimated from the spectral properties of the optical field generated by parametric mixing of ML with the applied pump radiation. Assuming uncorrelated optical fields, the linewidth of ML at $5.23 \mu\text{m}$ in rubidium vapor was estimated to be no more than 1.3 MHz, though this field has not been directly detected [26].

Recent theoretical work has demonstrated that coherent, directional light emission can also arise collectively from dense, arrays of subwavelength-spaced dipole-coupled emitters without the use of an optical resonator [27]. Such systems exhibit a transition from subradiant to superradiant emission accompanied by spectral narrowing, further underscoring the role of dipole-dipole interactions and collective coherence in free-space light generation.

In this broader context, superradiance refers to the cooperative spontaneous emission of phase-synchronized dipoles, producing an intensity that scales as N^2 and a decay rate enhanced by collective coupling [28–30]. While originally formulated for pulsed, fully inverted samples, related steady-state regimes can arise under CW driving, where long-range dipole correlations persist and

yield directional, phase-matched emission [31, 32]. These cooperative effects provide a natural framework for interpreting correlated bidirectional infrared emission in alkali vapors, bridging the gap between ASE-driven mirrorless lasing and genuine superradiant behavior.

A fundamental quantity for characterizing the statistical and coherence properties of a radiation source is the second-order intensity cross-correlation function $g_{1,2}^{(2)}(\tau)$ [33]. It is defined by

$$g_{1,2}^{(2)}(\tau) = \frac{\langle I_1(t) I_2(t + \tau) \rangle}{\langle I_1 \rangle \langle I_2 \rangle}, \quad (1)$$

where $I_1(t)$ and $I_2(t)$ denote the registered intensities at two distinct detection channels (e.g., a Hanbury Brown and Twiss setup [34, 35]). It reduces to the second-order autocorrelation $g^{(2)}(\tau)$, when $\langle I_1 \rangle$ and $\langle I_2 \rangle$ refer to the intensities of the same beam. The value $g^{(2)}(0)$ provides insight into the photon statistics and temporal coherence of the light source: (i) for coherent light (e.g., an ideal laser), $g^{(2)}(0) = 1$, indicating Poissonian photon statistics; (ii) for thermal light (e.g., from a blackbody or incandescent bulb), $g^{(2)}(0) = 2$, indicating photon bunching and super-Poissonian statistics; and for single-photon sources, $g^{(2)}(0) < 1$, indicating antibunching, a purely quantum phenomenon [33]. In Ref. [36], it was shown that the second-order correlation function $g^{(2)}(\tau)$ can reach values up to 2 for spontaneous decay processes when single-photon detectors are used.

It was shown that the intensity correlations of input beams can be partially transferred to generated forward-directed light via FWM in ^{85}Rb vapor [37]. The 420 nm collimated blue light inherits the bunching of the input fields, and the measured peak correlation $g^{(2)}(0)$ is significantly reduced due to Doppler broadening in the vapor and finite temporal resolution of the measurement.

Measurements of $g^{(2)}(\tau)$ revealed evidence of an oscillation, which might have been caused by periodic spiking in the intensity [38, 39]. Previous studies revealed complex temporal behavior in alkali vapors: Ref. [40] reported spiking dynamics in the emission from Rb atoms, whereas Ref. [41] demonstrated oscillatory behavior of the Pearson correlation coefficient between two signals in Na vapors. Given the linear relationship between the Pearson coefficient and the second-order correlation function, it is expected that $g^{(2)}(\tau)$ should also exhibit oscillatory behavior. This behavior of the intensity correlations has also been observed in hot Rb vapor, also in the presence of Doppler broadening, indicating that specific atomic velocity groups dominate the observed correlations [42].

While mirrorless lasing, ASE-driven gain, and directional emission in alkali vapors have been explored in a variety of contexts, quantitative measurements of the second-order coherence function for simultaneously forward- and backward-propagating mid-infrared emission remain comparatively scarce. Here, we characterize the temporal correlations of these counter-propagating

beams and identify a persistent oscillatory structure in $g^{(2)}(\tau)$ together with nontrivial cross-correlations. These observations indicate that the gain medium cannot be treated only as an amplified spontaneous emission, but instead also exhibits cooperative coupling between counter-propagating modes under threshold excitation. Thus, analysis of the shape and decay of $g^{(2)}(\tau)$ provides access to fundamental characteristics of the radiation, including coherence time, emission threshold, intensity noise, and the underlying light-matter interaction mechanisms.

II. EXPERIMENTAL SETUP AND PROCEDURES

The experimental setup is largely based on the one presented in Ref. [43]. Its simplified version, as well as relevant atomic transitions, are presented in Fig. 1.

The experiment employs a 10 cm long sodium vapor cell without buffer gas. The cell is mounted inside a magnetic shield composed of four-layers of μ -metal to suppress stray magnetic fields; a resistive heater consisting of a pair of twisted wires provides a controlled temperature gradient along the cell while ensuring reduced magnetic field noise. The temperature of the vapor cell is kept at 170°C throughout the experiment. The wedge-shaped angled windows of the cell help suppress optical feedback.

Two laser systems are used for excitation: a solid-state Toptica TA-SHG Pro laser operating at 589.2 nm resonant with the $3S_{1/2} \rightarrow 3P_{3/2}(F' = 3, 2, 1)$ transition, and a Coherent 899-21 dye laser at 569.0 nm, driving the $3P_{3/2} \rightarrow 4D_{5/2}$ transition. Efficient ground-state repumping, which lowers the ASE threshold and enhances excitation efficiency [44], is achieved by generating spectral sidebands at 1.713 GHz via frequency modulation of the 589.2 nm laser using an electro-optic modulator (EOM) with a modulation depth of -12 dBm. The outputs of the two lasers are combined on a non-polarizing beam splitter to form a bichromatic excitation beam, which is directed into the sodium cell with a minimum spot diameter of approximately 1 mm. The polarization and intensity of both the 589.2 nm and 569.0 nm components are controlled using waveplates and polarizers.

Mid-infrared emission directed along the laser field propagation direction at 2.21 μm and 2.34 μm is detected with VIGO LabM-I-10.6 photodetector (PD), and data acquired is registered by a data acquisition (DAQ) system with 500 MS/s. We also observe backward emission at 2.21 μm and at 2.34 μm . However, the intensity of the 2.34 μm backward emission is too weak to be reliably detected and analyzed at the same experimental conditions, and therefore it is not further considered in this work. Forward and backward emissions at 2.21 μm are simultaneously measured using two PDs, with each radiation recorded on a two-channel DAQ card. For the laser light measurements, we employ a Thorlabs PDA10A pho-

todetector, as the VIGO detector is not sensitive to the laser wavelengths used.

With 589.2 nm light at 230 mW and 569.0 nm light at 45 mW, we observe 80 μW of the 2.21 μm collimated light in the forward direction and 45 μW in the backward direction. The registered signals exhibit temporal spiking and pronounced oscillations are visible in the traces (see inset in Fig. 2a, and Appendix A).

III. RESULTS AND DISCUSSIONS

To verify the approach for extracting the second-order correlation functions, we first measure the intensity of CW lasers at 569.0 nm and 589.2 nm and calculate the $g^{(2)}(\tau)$ functions, shown in dotted green and solid yellow lines, respectively, in Fig. 2. The deviation of $g^{(2)}(0)$ from the expected value of 1 is less than 10^{-4} for both lasers. All measurements were carried out over a total acquisition time of 500 ms. The recorded intensity traces were partitioned into 1000 equal segments, and the second-order correlation function $g^{(2)}(\tau)$ was evaluated for each segment and then averaged.

With the same technique (but using the VIGO LabM-I-10.6 detector), we recorded the emission at 2.21 μm in both forward and backward directions simultaneously, as well as the forward-directed emission at 2.34 μm . Figure 2(a) shows the results for the 2.21 μm emission, with the forward-directed radiation represented by a solid line and the backward-directed radiation by a dashed line. A part of time-dependent raw normalized intensities is shown in Fig. 2(a) inset, with the forward-directed radiation plotted by solid and the backward-directed radiation by dashed lines, revealing periodic spike structure. Figure 2(b) displays the forward-directed emission at 2.34 μm by a solid line. The standard errors are smaller than the line thickness and are invisible in the figures. An example of $g^{(2)}(\tau)$ calculation from a single segment is presented in Appendix A. All data correspond to an incident pump power of 15 mW at 569.0 nm and 230 mW at 589.2 nm. As seen in the figure, $g^{(2)}(0) > 1$, indicating photon bunching and demonstrating that the observed "mirrorless lasing" does not correspond to pure lasing, but rather contains at least an admixture of ASE. Using Eq. (3.8.7) from [33], the expected value of $g^{(2)}(0)$ for a single-mode signal is expected to be approximately ~ 1.78 for chaotic light, given a coherence time of ~ 20 ns, and an integration time of 8 ns. However, our measured value is significantly lower.

On the other hand, sub-thermal values $1 < g^{(2)}(0) < 2$ can arise from the detection of multiple independent spatio-temporal modes and finite measurement bandwidth (integration time) [45]. For mutually incoherent chaotic modes, one expects $g^{(2)}(0) = 1 + 1/M$, where M is the number of effective modes [46].

The calculated cross-correlations between the 2.21 μm forward- and backward-emitted light is shown in Fig. 2(c) with a solid curve. For reference, the figure includes the

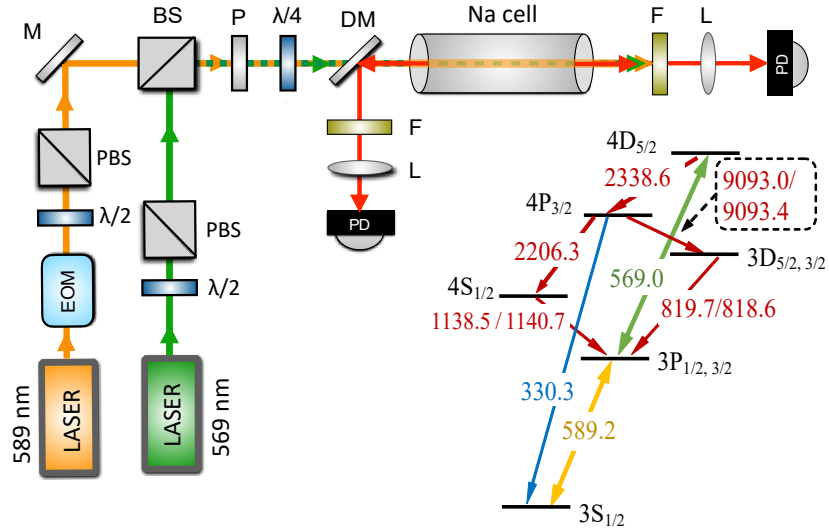


FIG. 1. Schematic top view of the experimental setup on the left. EOM: Electro-optic modulator driven at 1.713 GHz, PBS: Polarizing beam splitter, BS: Non-polarizing beam splitter, M: Mirror, P: Polarizer, DM: Dichroic mirror, F: Infrared Filter, L: Lens, PD: Photodetector. Relevant Na energy levels and transitions are presented on the right.

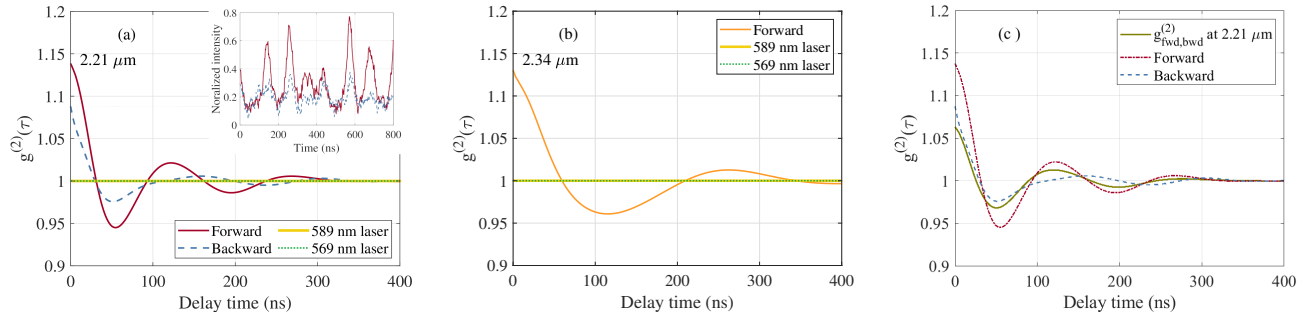


FIG. 2. Autocorrelation functions vs. delay time τ for 589.2 nm laser (solid horizontal line), 569.0 nm laser (dotted horizontal line), (a) forward (solid) and backward (dashed) emission at $2.21 \mu\text{m}$, and (b) forward emission at $2.34 \mu\text{m}$. (c) Cross-correlation vs. delay time τ in solid line between forward and backward emitted lights at $2.21 \mu\text{m}$. For reference, $2.21 \mu\text{m}$ forward (dash-dotted), and backward (dashed) auto-correlations are shown. The 569.0 nm laser power is 15 mW, the 589.2 nm laser power is 230 mW.

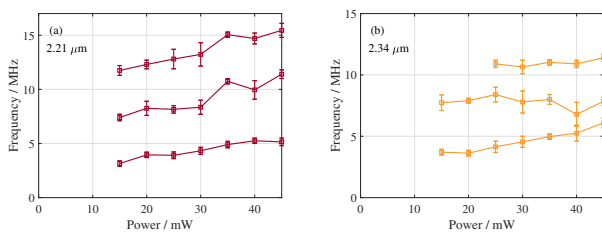


FIG. 3. Dependence of emitted radiation oscillation frequencies on 569.0 nm laser power for forward emitted (a) $2.21 \mu\text{m}$ and (b) $2.34 \mu\text{m}$ fields. 589.2 nm laser power is fixed at 230 mW.

auto-correlations of the forward (dash-dotted) and backward (dashed) $2.21 \mu\text{m}$ emissions. The cross-correlation between the forward- and backward-emitted $2.21 \mu\text{m}$ light takes values between one and two. This positive

cross-correlation between forward and backward channels implies that the two counterpropagating fields are linked through a common macroscopic polarization of the ensemble. This behavior is inconsistent with independent ASE channels, which would yield statistically uncorrelated emission. The correlated infrared radiation observed under continuous two-color excitation, therefore, signals the emergence of a collective, phase-matched radiative process. In this regime, the driving fields imprint a spatially coherent polarization grating across the vapor, leading to constructive interference of the emitted dipole fields along phase-matched directions. The resulting directional enhancement constitutes a CW cooperative emission closely related to superradiance[31]. In contrast to the transient Dicke-type superradiant burst following pulsed inversion, the CW-driven sodium system reaches a steady state in which long-range dipole correlations persist and radiate coherently into both forward

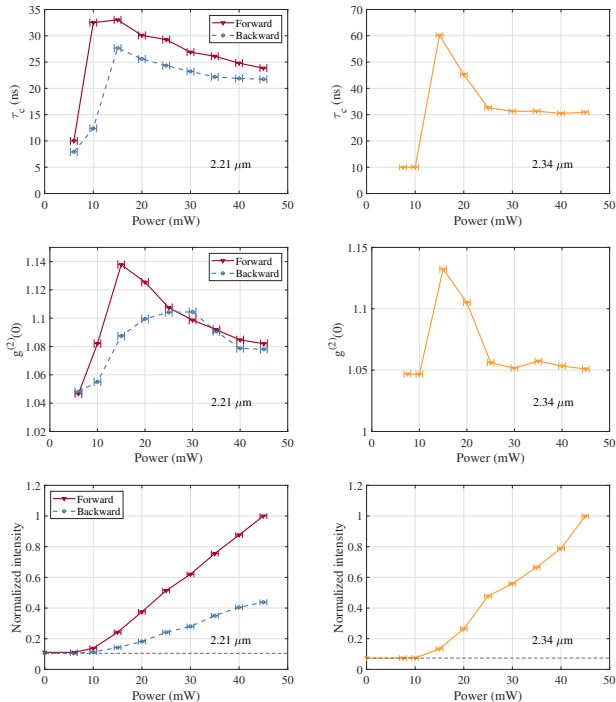


FIG. 4. Coherence time (top), $g^{(2)}(0)$ (middle), normalized mean intensity (bottom) of forward (solid) and backward (dashed) emission (left pane); and 2.34 μm emitted light (right pane) dependence on 569.0 nm laser power. 589.2 nm laser power is 230 mW. Horizontal error bars indicate the uncertainty of the laser power (± 0.7 mW) due to power fluctuations.

and backward modes.

In the dependence on delay time of auto-correlations and cross-correlations, oscillatory behavior is observed. A pronounced oscillation with a period of around 120 ns, which is equivalent to 8.3 MHz, is already apparent from the signal structure itself, which is translated to the time-dependence of $g^{(2)}(\tau)$ (see Fig. 2a, solid line). Additional, less obvious components are deduced using the Fourier transform of the signal and the corresponding $g^{(2)}(\tau)$ function, which yielded consistent spectral features. Oscillation frequencies are presented in Fig. 3 as a function of 569.0 nm laser power, 589.2 nm laser power is fixed at 230 mW.

Across the range of pump powers investigated, we observe persistent oscillations around 4–5, 8–11, and 12–16 MHz, see Fig. 3. The systematic upshift of these frequencies with increasing power is consistent with light-induced (AC Stark) shifts of the relevant energy splittings (see Appendix B).

Another possible reason for oscillations is the dynamical buildup of emission, arising from the competition between time-coherent mirrorless lasing and ASE processes [38, 39], although in contrast to the results reported in these papers, we do not observe damping of the oscillations far away from the emission threshold.

Figure 4 summarizes the dependence of several statistical properties of the forward- and backward-emitted radiation on the 569.0 nm pump power. The 589.2 nm laser power was held constant at 230 mW. The left column corresponds to emission at 2.21 μm and the right column to emission at 2.34 μm . In each column, the top panel displays the coherence time τ_c , the middle panel shows the zero-delay intensity autocorrelation $g^{(2)}(0)$, and the bottom panel reports the normalized mean intensity of the detected directional emission. For the 2.21 μm radiation, we plot forward-directed and backward-directed emissions for direct comparison (solid and dotted traces, respectively); the 2.34 μm emission is shown in the right column. All quantitative fits shown in Fig. 4 include statistical uncertainties. The y -axis uncertainties lie within the symbol size and are therefore not visible, whereas the uncertainty in the laser power is estimated as ± 0.7 mW, and this is reflected in the horizontal error bars of the plots.

All measured beams exhibit qualitatively similar behavior as a function of the 569.0 nm pump power: no directional emission is detected below a pump threshold near $P_{569} \simeq 7$ mW, while above the threshold, the signals grow and their statistical properties evolve. We note that several different nonlinear optical mechanisms can display threshold-like onsets (e.g. ASE, FWM, and ML).

The coherence time τ_c was extracted by fitting the measured correlation function $g^{(2)}(\tau)$ with a Gaussian profile and taking the $1/e$ decay width as τ_c [33]. The coherence time reaches a maximum at $P_{569} \approx 15$ mW for all recorded beams, and for larger powers, it approaches approximately 20 ns for the 2.21 μm emission and ~ 30 ns for the 2.34 μm emission. The value of $g^{(2)}(0)$ likewise evolves with 569.0 nm pump power and asymptotes to a nearly constant value: for the 2.34 μm emission, this occurs already at $P_{569} \approx 25$ mW, whereas for the 2.21 μm emission, the asymptotic behavior is reached at higher pump powers, ~ 40 mW. For the 2.21 μm emission, $g^{(2)}(0)$ rises from about 1.04 at threshold to a peak value of 1.14 before settling to 1.08 at higher powers, while for the 2.34 μm emission, it follows a similar trend, peaking at 1.13 and stabilizing near 1.05. Such small deviations above unity are consistent with nearly coherent (laser-like) emission, but with a weak excess of super-Poissonian fluctuations that likely arise from residual amplified spontaneous emission or parametric contributions.

The tendency of both τ_c and $g^{(2)}(0)$ to level off at high 569.0 nm pump power is consistent with the system reaching a steady-state regime in which the dominant gain and loss processes balance; this behaviour is expected for both chaotic source [$g^{(2)}(0) = 2$] and a laser [$g^{(2)}(0) = 1$].

The mean detected intensity of the directional emission exhibits a clear threshold near $P_{569} \approx 10$ mW, see Fig. 4, bottom row. Below this value, the signal remains constant at the detector offset level (indicated by the thin black dashed line). Above the threshold, the intensity in-

creases linearly with pump power, indicating the onset of gain-dominated directional emission.

IV. CONCLUSION

In summary, we have investigated the statistical properties of sodium emission under bichromatic excitation by analyzing the second-order intensity correlation function $g^{(2)}(\tau)$. The directional emissions at 2.21 and 2.34 μm exhibit $g^{(2)}(0)$ values between one and two, together with strong forward–backward correlations and persistent oscillations, pointing to a phase-matched, steady-state cooperative emission regime. These observations are consistent with CW directional superradiance [31], in which synchronized dipoles radiate coherently into both counterpropagating modes. Such behavior naturally accommodates the measured subthermal statistics and the presence of multiple effective modes, as partial mode averaging reduces the observed bunching amplitude without destroying collective coherence.

Throughout the explored range of pump powers, $g^{(2)}(\tau)$ of the emissions exhibited persistent oscillations at characteristic frequencies near 4–5, 8–11, and 12–16 MHz, with a systematic upshift of these components at higher excitation power. It is consistent with AC Stark shifts of the underlying hyperfine sublevels participating in the cooperative polarization, a mechanism analogous to multi-mode superradiant beating.

This behavior can be placed in a broader context: in photon Bose–Einstein condensation the mode populations follow a Bose–Einstein distribution, and the growth of the macroscopic ground-state occupation is reflected in the second-order correlation function $g^{(2)}(\tau)$, which tracks the crossover from thermal to coherent behavior. Near threshold the condensate may still exhibit bunching with $g^{(2)}(0) > 1$ due to reservoir-induced number fluctuations, while in a well-developed condensate the ideal expectation is $g^{(2)}(0) \approx 1$, signifying second-order coherence [47]. Although directional scattering and photon condensation arise from distinct physical

mechanisms—non-equilibrium amplification versus equilibrium condensation—both phenomena can be characterized by their photon correlations. In this sense, $g^{(2)}(\tau)$ offers a unifying diagnostic for identifying thermal, amplified, and condensed regimes of light, even though the statistical origins of coherence differ.

In addition, the backward-emitted light offers promising opportunities for laser guide star generation and mesospheric remote sensing, and our $g^{(2)}$ analysis provides valuable insight into the coherence and mode structure of this emission, paving the way for the optimization of sodium-based light sources for atmospheric and astronomical applications. Looking ahead, extending these studies to more complex excitation geometries and structured light fields could provide further insight into the interplay between coherence, polarization, and spatial mode structure. In particular, measuring quantum correlations in polychromatic radiation generated by twisted light carrying orbital angular momentum (OAM) represents a promising direction for future research.

ACKNOWLEDGEMENTS

Authors acknowledge helpful discussions with M. Chekhova, M. Fleischhauer, J. Marino, H. Ritsch, S. Malinovskaya, A. Nomerotski, H. Karapetyan, A. Wickenbrock, H. Bekker, M. Khanbekyan, E. Klinger.

FUNDING

This work was supported by the Higher Education and Science Committee of the Republic of Armenia (Research projects N24-2PTS-1C003 and N24-2PTS-1C004), through the QuantERA II Program, with funding received via the EU H2020 research and innovation program under Grant No. 101017733 and associated support from the German VDI under Grant No. 13N16931 (V-MAG), project HEU-RIA-MUQUABIS Grant No. 101070546.

-
- [1] D. C. Hanna, M. A. Yuratich, and D. Cotter, *Nonlinear Optics of Free Atoms and Molecules* (Springer, 1979).
- [2] D. Budker, W. Gawlik, D. F. Kimball, S. M. Rochester, V. V. Yashchuk, and A. Weis, Resonant nonlinear magneto-optical effects in atoms, *Reviews of Modern Physics* **74**, 1153 (2002).
- [3] G. A. Pitz and M. D. Anderson, Recent advances in optically pumped alkali lasers, *Applied Physics Reviews* **4**, 041101 (2017), https://pubs.aip.org/aip/apr/article-pdf/doi/10.1063/1.5006913/14574029/041101_1_online.pdf.
- [4] P. P. Sorokin, N. S. Shiren, J. R. Lankard, E. C. Hammond, and T. G. Kazyaka, Stimulated electronic raman scattering, *Applied Physics Letters* **10**, 44 (1967), https://pubs.aip.org/aip/apl/article-pdf/10/2/44/18419635/44_1_online.pdf.
- [5] C.-S. Wang, Theory of stimulated raman scattering, *Phys. Rev.* **182**, 482 (1969).
- [6] R. W. Boyd, M. S. Malcuit, D. J. Gauthier, and K. Rzaewski, Competition between amplified spontaneous emission and the four-wave-mixing process, *Phys. Rev. A* **35**, 1648 (1987).
- [7] D. Grischkowsky, J. Lankard, and P. Sorokin, An atomic rydberg state 16- μ laser, *IEEE Journal of Quantum Electronics* **13**, 392 (1977).
- [8] Y. Sebbag, Y. Barash, and U. Levy, Generation of coherent mid-ir light by parametric four-wave mixing in alkali vapor, *Optics Letters* **44**, 971 (2019).

- [9] P. Londero, V. Venkataraman, A. R. Bhagwat, A. D. Slepko, and A. L. Gaeta, Ultralow-power four-wave mixing with Rb in a hollow-core photonic band-gap fiber, *Physical Review Letters* **103**, 043602 (2009).
- [10] B. Zhdanov, M. Shaffer, and R. Knize, Diode pumped alkali lasers: history, current state and perspectives, in *Conference on Lasers and Electro-Optics 2011* (2011) p. CThA5.
- [11] A. V. Andreev, V. I. Emel'yanov, and Y. A. Il'inskii, *Cooperative Effects in Optics: Superradiance and Phase Transitions* (Institute of Physics Publishing, Bristol and Philadelphia, 1993).
- [12] H. Cao, Lasing in random media, *Waves in Random Media* **13**, R1 (2003), <https://doi.org/10.1088/0959-7174/13/3/201>.
- [13] S. Dubey, G. A. Kazakov, B. Heizenreder, S. Zhou, S. Bennetts, S. A. Schäffer, A. Sitaram, and F. Schreck (MoSaiQC Collaboration), Modeling of a continuous superradiant laser on the sub-mhz $^1s_0 \rightarrow ^3p_0$ transition in neutral strontium-88, *Phys. Rev. Res.* **7**, 013292 (2025).
- [14] Z. Zhang, F. Zhang, B. Xu, H. Xie, B. Fu, X. Lu, N. Zhang, S. Yu, J. Yao, Y. Cheng, and Z. Xu, High-sensitivity gas detection with air-lasing-assisted coherent raman spectroscopy, *Ultrafast Science* **2022**, 9761458 (2022).
- [15] K.-M. C. Fu, G. Z. Iwata, A. Wickenbrock, and D. Budker, Sensitive magnetometry in challenging environments, *AVS Quantum Science* **2**, 044702 (2020), https://pubs.aip.org/avs/aqs/article-pdf/doi/10.1116/5.0025186/19738954/044702_1_online.pdf.
- [16] A. M. Akulshin, D. Budker, F. Pedreros Bustos, T. Dang, E. Klinger, S. M. Rochester, A. Wickenbrock, and R. Zhang, Remote detection optical magnetometry, *Physics Reports* **1106**, 1 (2025), remote Detection Optical Magnetometry.
- [17] S. Jacobs, G. Gould, and P. Rabinowitz, Coherent light amplification in optically pumped cs vapor, *Phys. Rev. Lett.* **7**, 415 (1961).
- [18] P. P. Sorokin and J. R. Lankard, Infrared lasers resulting from photodissociation of cs₂ and Rb₂, *The Journal of Chemical Physics* **51**, 2929 (1969), https://pubs.aip.org/aip/jcp/article-pdf/51/7/2929/18863937/2929_1_online.pdf.
- [19] A. Sharma, N. D. Bhaskar, Y. Q. Lu, and W. Happer, Continuous-wave mirrorless lasing in optically pumped atomic cs and Rb vapors, *Applied Physics Letters* **39**, 209 (1981), https://pubs.aip.org/aip/apl/article-pdf/39/3/209/18444263/209_1_online.pdf.
- [20] A. Papoyan, S. Shmavonyan, A. Khanbekyan, H. Azizbekyan, M. Movsisyan, G. Bao, D. Kanta, A. Wickenbrock, and D. Budker, Evidence for degenerate mirrorless lasing in alkali metal vapor: forward beam magneto-optical experiment, *Journal of Physics B: Atomic, Molecular and Optical Physics* **52**, 195003 (2019).
- [21] A. Akulshin, D. Budker, and R. McLean, Directional infrared emission resulting from cascade population inversion and four-wave mixing in Rb vapor, *Opt. Lett.* **39**, 845 (2014).
- [22] A. M. Akulshin, F. P. Bustos, and D. Budker, Continuous-wave mirrorless lasing at 2.21 μm in sodium vapors, *Opt. Lett.* **43**, 5279 (2018).
- [23] D. Antypas, O. Tretiak, D. Budker, and A. Akulshin, Polychromatic, continuous-wave mirrorless lasing from monochromatic pumping of cesium vapor, *Opt. Lett.* **44**, 3657 (2019).
- [24] A. Ramaswamy, J. Chathanathil, D. Kanta, E. Klinger, A. Papoyan, S. Shmavonyan, A. Khanbekyan, A. Wickenbrock, D. Budker, and S. A. Malinovskaya, Mirrorless lasing: A theoretical perspective, *Optical Memory and Neural Networks* **32**, S443 (2023).
- [25] A. Ramaswamy and S. A. Malinovskaya, Degenerate mirrorless lasing in thermal alkali vapors, arXiv preprint 10.48550/arXiv.2503.14705 (2025), arXiv:2503.14705 [physics.atom-ph].
- [26] A. Akulshin, C. Perrella, G.-W. Truong, A. Luiten, D. Budker, and R. McLean, Linewidth of collimated wavelength-converted emission in Rb vapour, *Applied Physics B* **117**, 203 (2014).
- [27] A. Bychek, R. Holzinger, and H. Ritsch, Nanoscale mirrorless superradiant lasing, *Phys. Rev. Lett.* **135**, 143601 (2025).
- [28] R. H. Dicke, Coherence in spontaneous radiation processes, *Phys. Rev.* **93**, 99 (1954).
- [29] N. E. Rehler and J. H. Eberly, Superradiance, *Phys. Rev. A* **3**, 1735 (1971).
- [30] G. Ferioli, A. Glicenstein, F. Robicheaux, R. T. Sutherland, A. Browaeys, and I. Ferrier-Barbut, Laser-driven superradiant ensembles of two-level atoms near dicke regime, *Phys. Rev. Lett.* **127**, 243602 (2021).
- [31] G. Ferioli, I. Ferrier-Barbut, and A. Browaeys, Emergence of second-order coherence in the superradiant emission from a free-space atomic ensemble, *Phys. Rev. Lett.* **134**, 153602 (2025).
- [32] S. Agarwal, E. Chaparro, D. Barberena, A. P. n. Orioli, G. Ferioli, S. Pancaldi, I. Ferrier-Barbut, A. Browaeys, and A. Rey, Directional superradiance in a driven ultracold atomic gas in free space, *PRX Quantum* **5**, 040335 (2024).
- [33] R. Loudon, *The Quantum Theory of Light*, 2nd ed. (Clarendon Press, Oxford, 1983).
- [34] R. H. Brown and R. Q. Twiss, Correlation between photons in two coherent beams of light, *Nature* **177**, 27 (1956).
- [35] R. J. Glauber, The quantum theory of optical coherence, *Physical Review* **130**, 2529 (1963).
- [36] F. T. Arecchi, E. Courtens, R. Gilmore, and H. Thomas, Atomic coherent states in quantum optics, *Phys. Rev. A* **6**, 2211 (1972).
- [37] Y. S. Ihn, K.-K. Park, Y. Kim, Y.-T. Chough, and Y.-H. Kim, Intensity correlation in frequency upconversion via four-wave mixing in rubidium vapor, *J. Opt. Soc. Am. B* **34**, 2352 (2017).
- [38] J. Wiersig, C. Gies, F. Jahnke, M. Aßmann, T. Berstermann, M. Bayer, C. Kistner, S. Reitzenstein, C. Schneider, S. Höfling, A. Forchel, C. Kruse, J. Kalden, and D. Hommel, Direct observation of correlations between individual photon emission events of a microcavity laser, *Nature* **460**, 245 (2009).
- [39] T. Wang, G. P. Puccioni, and G. L. Lippi, Dynamical buildup of lasing in mesoscale devices, *Scientific Reports* **5**, 15858 (2015).
- [40] A. M. Akulshin, N. Rahaman, S. A. Suslov, D. Budker, and R. J. McLean, Spiking dynamics of frequency upconverted field generated in continuous-wave excited rubidium vapors, *J. Opt. Soc. Am. B* **37**, 2430 (2020).
- [41] A. Akulshin, F. P. Bustos, and D. Budker, Intensity-correlated spiking of infrared and ultraviolet emission from sodium vapors, *Opt. Lett.* **46**, 2131 (2021).

- [42] A. A. C. de Almeida, A. S. Alvarez, N. R. de Melo, M. R. L. da Motta, M. P. M. de Souza, and S. S. Vianna, Intensity correlations in transmission and four-wave-mixing signals intermediated by hot rubidium atoms, *Phys. Rev. A* **111**, 043518 (2025).
- [43] A. M. Akulshin, F. P. Bustos, N. Rahaman, and D. Budker, Origin and properties of polychromatic directional emission from sodium atoms, *J. Opt. Soc. Am. B* **40**, 3276 (2023).
- [44] A. M. Akulshin, A. A. Orel, and R. J. McLean, Collimated blue light enhancement in velocity-selective pumped Rb vapour, *Journal of Physics B: Atomic, Molecular and Optical Physics* **45**, 015401 (2011).
- [45] J. Mika, L. Podhora, L. Lachman, P. Obšil, J. Hloušek, M. Ježek, R. Filip, and L. Slodička, Generation of ideal thermal light in warm atomic vapor, *New Journal of Physics* **20**, 093002 (2018).
- [46] J. W. Goodman, *Statistical Optics*, 2nd ed. (Wiley, Hoboken, NJ, 2015).
- [47] J. Schmitt, T. Damm, D. Dung, F. Vewinger, J. Klaers, and M. Weitz, Observation of grand-canonical number statistics in a photon bose-einstein condensate, *Phys. Rev. Lett.* **112**, 030401 (2014).
- [48] E. Arimondo, M. Inguscio, and P. Violino, Experimental determinations of the hyperfine structure in the alkali atoms, *Rev. Mod. Phys.* **49**, 31 (1977).
- [49] F. Biraben and K. Beroff, Hyperfine interaction in the 4d32 and the 4d52 levels of sodium, *Physics Letters A* **65**, 209 (1978).
- [50] B. Burghardt, M. Dubke, W. Jitschin, and G. Meisel, Sub-natural linewidth laser spectroscopy of doppler-free two-photon resonances, *Physics Letters A* **69**, 93 (1978).

Appendix A: Temporal structure and auto- and cross-correlation functions

In order to illustrate the temporal dynamics of the detected mid-infrared emission, we present the raw intensity traces of the $2.21\ \mu\text{m}$ radiation in both forward and backward directions under excitation with 230 mW at 589.2 nm and 45 mW at 569.0 nm. The time-dependent intensities are shown in Fig. 5(a), with the forward-directed radiation plotted by solid and the backward-directed radiation by dashed lines. The radiations clearly exhibit spike-like structures in both the forward and backward directions, which appear largely in phase, indicating a strong correlation between the two emissions. The mean of the signals of the forward and backward emissions is in the order of $\sim 10^3$, and variance is in the order of $\sim 10^5$.

The corresponding second-order correlation functions, calculated directly from these data, are presented in Fig. 5(b). Here, the dash-dotted line corresponds to the forward emission, the dashed line to the backward emission, and the solid curve to the cross-correlation between

the two. These results provide a representative example of the raw data underlying the correlation analysis and demonstrate the presence of correlated fluctuations between forward- and backward-propagating emissions at $2.21\ \mu\text{m}$.

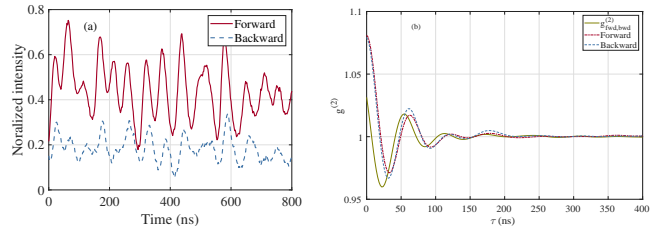


FIG. 5. (a) Time dependence of the detected intensities at $2.21\ \mu\text{m}$ in the forward (solid) and backward (dashed) directions, recorded with laser powers of 230 mW at 589.2 nm and 45 mW at 569.0 nm. (b) Corresponding second-order auto-correlation functions $g^{(2)}(\tau)$ calculated from the same data: forward emission (dash-dotted line), backward emission (dashed line), and forward-backward cross-correlation (solid).

Appendix B: Hyperfine splittings of relevant states

As discussed in the main text, the temporal structure of the registered emission signals reveals several characteristic frequency components. Across the investigated 569.0 nm laser power range, we observe persistent oscillations in $g^{(2)}(\tau)$ around 4–5, 8–11, and 12–16 MHz. For comparison, the hyperfine splittings of the $4D_{3/2,5/2}$, $4P_{1/2,3/2}$, and $4S_{1/2}$ states were estimated using data from Refs. [48–50], and the corresponding energy separations ΔF are summarized in Table I. The highlighted row indicates the transitions whose hyperfine differences most closely match the observed oscillation frequencies, suggesting that these arise from beatings between the respective sublevels. Discrepancies can be attributed to AC Stark shifts, finite accuracy of hyperfine constants, and experimental factors such as detection bandwidth, residual magnetic fields, and multimode coupling.

ΔF	1-0	2-1	3-2	4-3
$4D_{3/2}$	0.23	0.46	0.69	×
$4D_{5/2}$	×	0.056	0.084	0.11
$4P_{1/2}$	×	54	×	×
$4P_{3/2}$	5.1	11.2	19.3	×
$4S_{1/2}$	×	404	×	×

TABLE I. Estimated hyperfine splittings ΔF for the $4D_{3/2,5/2}$, $4P_{1/2,3/2}$, and $4S_{1/2}$ states of sodium. The highlighted row indicates transitions whose hyperfine separations correspond most closely to the oscillation frequencies observed in $g^{(2)}(\tau)$.